


Atmospheric clearing of solid-particle debris using femtosecond filaments

Kyle S. Latty¹* and Kyle C. Hartig¹

Nuclear Engineering Program, Department of Materials Science and Engineering, University of Florida, Gainesville, Florida 32611, USA

 (Received 2 April 2024; accepted 9 July 2024; published 29 July 2024)

Through nonlinear self-focusing, femtosecond pulses can propagate several kilometers beyond diffraction limits, forming an ionization channel in air known as a laser filament. It has been demonstrated that in the wake of the filament, aerosols can be effectively cleared to improve the transmission of subsequent laser pulses or secondary light sources, pertinent to applications in atmospheric sensing. However, the current understanding of aerosol clearing is founded on interactions with droplets to simulate fogs and clouds and thus does not extend to solid particles or atmospheric debris. Using optical trapping, we isolate both graphite and silica microparticles and directly measure the subsequent displacement caused by the filament using time-resolved shadowgraphy. The shock wave from the filament is demonstrated to propel particles away from the filament, directly contributing to atmospheric debris clearing. Particles exposed to the laser light in either the intense filament core or the surrounding energy reservoir are axially displaced along the beam path. It is found that the optomechanical properties of the particle largely influence the axial displacement induced by laser exposure through mechanisms such as radiation pressure, mass ejection from ablation or optical damage, and particle deagglomeration.

DOI: [10.1103/PhysRevApplied.22.014075](https://doi.org/10.1103/PhysRevApplied.22.014075)

I. INTRODUCTION

Femtosecond lasers show promise as a means of achieving stand-off atmospheric sensing through the formation of laser filaments. Filamentation typically occurs through the propagation of high-power ultrashort pulses in a transparent medium to achieve nonlinear self-focusing [1]. For air propagation, self-focusing causes the pulse intensity to gradually increase, eventually resulting in the ionization of air species to form a weak plasma that begins to defocus the pulse. The dynamic balance between nonlinear self-focusing and plasma defocusing creates a weakly ionized plasma channel in air known as a laser filament, consisting of two distinct regions: (1) the high-intensity filament core, approximately 80–100 μm in diameter, capable of causing photoionization of air species to induce plasma formation [2,3], and (2) the low-intensity energy reservoir surrounding the filament core that retains most of the pulse energy and actively restores the energy lost in the filament core [4,5]. The intensity of the filament core is clamped given the sustained balance between self-focusing and plasma defocusing and is sufficiently intense to excite aerosols to facilitate emission spectroscopy techniques [6–9]. Along with filament-induced particle emissions, the self-transforming white light generated through self-phase modulation is well suited for light detection and ranging

(LIDAR) to measure absorption and scattering from air species for the purpose of atmospheric monitoring [10–13].

An underlying challenge of atmospheric monitoring using filaments or other laser-based techniques is the energy losses that accrue through scattering and absorption with atmospheric particles, attenuating light delivery and light collection at longer distances. Clouds and fogs consisting of micrometer-sized droplets are a common scattering medium in the atmosphere, inspiring several investigations dedicated to understanding the dynamics of filamentation in aerosolized environments. Filaments have been shown to survive interactions with large droplets that occlude the majority of the filament core, indicating laser filaments can persist through atmospheric attenuation as long as sufficient power resides in the energy reservoir to support self-focusing in the filament core [14–16]. In the wake of the passing filament, aerosols in the vicinity of the filament are cleared for several milliseconds, resulting in a unique fog-clearing hysteresis effect that can be quasistained using high-repetition-rate pulse trains (>200 Hz) to improve the transmission of subsequent pulses or secondary light sources [17–20]. Fog clearing has also been achieved using coherently controlled molecular quantum wakes using a stacked femtosecond-pulse train tuned to the molecular rotation of N_2 , without having to generate a plasma through filamentation [21,22].

*Contact author: klatty@ufl.edu

In regard to the physical mechanism driving fog clearing, several studies have shown that micrometer-sized droplets behave similarly to a focusing lens, where laser light is internally focused due to refraction occurring at the irradiated surface [23–25]. In the higher-intensity filament core, internal ablation can occur within the droplet volume, to form a rapidly expanding microcavity that bursts the droplet through optical shattering, feasibly improving transmission of subsequent pulses by reducing light scattering from larger particle surfaces [26,27]. This concept has recently been extended to the region of the energy reservoir, where 5 μm droplets in the energy reservoir are also shown to undergo a weaker shattering effect at the rear surface of the droplet, managing to cause backward displacement by several hundred micrometers relative to the beam axis [28].

Unlike particle interactions that occur from exposure to the laser pulse, transverse displacement of particles away from the filament results from the pressure of the expanding plasma shock wave [29–31]. Recently, optically trapped silica microspheres have been shown to experience forces on the order of nanonewtons at distances upward of 5 mm away from the filament due to shock-wave interactions [32]. The shock wave expands by several millimeters and thus serves as the only applicable displacement mechanism of particles beyond the boundaries of energy reservoir, with a diameter typically on the order of a millimeter. Unlike the axial displacement of droplets through optical shattering, the transverse particle displacement induced by the shock wave directly propels particles away from the beam path. Intuitively, while the shock wave may appear to impact fog clearing more significantly, the relative contribution to fog clearing from laser-particle and shock-wave-particle clearing mechanisms is difficult to quantify in isolation, as the two phenomena occur simultaneously. Furthermore, given that optical shattering greatly depends on the optomechanical properties of the particle interactive with the laser pulse, the displacement magnitude and vector for particles other than water droplets remains unclear. Thus, the clearing behavior of filaments interacting with atmospheric aerosols containing solid particles (e.g., sand, snow, soot, pollen, nuclear fallout, etc.) is largely a topic of conjecture.

In this study, optical trapping is used to isolate solid particles with sizes ranging from 2 to 6 μm positioned near a passing femtosecond filament. Both graphite and silica microparticles are trapped and studied to represent the cases of absorptive and transparent particles in the atmosphere, respectively. Time-resolved shadowgraphy is used to measure the particle displacement of 200 μs after interacting with the filament and the original position of the trapped particle is varied relative to the location of the filament core. The evolution of the filament shock wave is also captured using shadowgraph images to determine the position of the shock wave, where the shock wave is observed

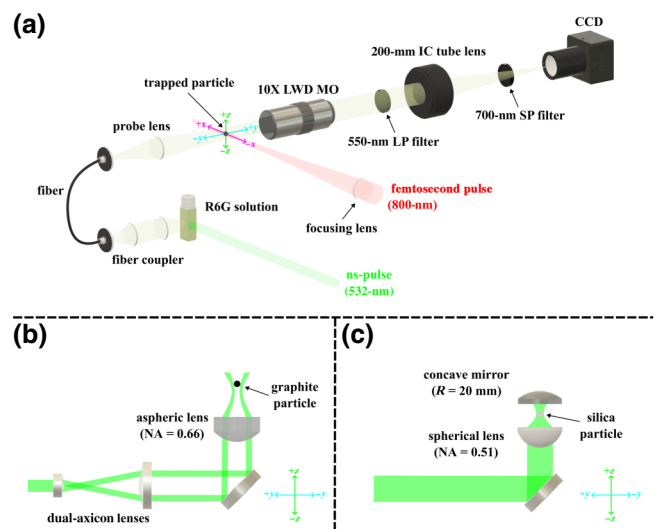


FIG. 1. (a) The simplified experimental setup used to measure particle displacement using time-resolved shadowgraphy. (b) A vertical hollow beam is generated using dual-axicon lenses to trap graphite particles. (c) A vertical confocal Gaussian beam generated using a concave mirror is used to trap silica particles.

exceeding the boundaries of the energy reservoir within the first 1 μs . The shock wave is confirmed to induce transverse particle displacement away from the filament, even for particles located outside the boundaries of the energy reservoir. We have found that filaments can clear solid particles through several mechanisms, including shock-wave pressure, radiation pressure, particle deagglomeration, and mass ejection caused by mechanical damage to the particle morphology through optical damage and ablation.

II. EXPERIMENTAL METHODS

A. Time-resolved shadowgraphy

A simplified schematic of the experimental setup is shown in Fig. 1(a). A chirped pulse amplified Ti:sapphire laser (Coherent Astrella) is used to generate 60-fs pulses at a center wavelength of 800 nm. The pulse energy is adjusted to 3.6 mJ, yielding a peak power of 32 GW, exceeding the critical power for self-focusing in air (P_{cr}) by a factor of 6 [1]. Using a burn paper, only a single burn mark is found at the center using a 1-m focusing lens, indicating that only a single filament is being formed with each laser pulse [33]. The repetition rate of the pulse train is set to 10 Hz, to cleanly pass a single pulse through an optical shutter with an opening time of 6 ms (Uniblitz VS25, Vincent Associates).

Time-resolved shadowgraphy of trapped particles is performed using the fluorescence from a dilute Rhodamine 6G (R6G) ethanol solution as probe source, pumped using a Q-switched Nd:YAG laser (Surelite-II, Amplitude) with the fundamental wavelength frequency doubled to 532 nm.

The short-lived fluorescence of R6G produces shadowgraph images free of coherence artifact noise with time resolutions comparable to the pulse duration of the pump laser. Given that the pulse duration of the Nd:YAG laser is 7 ns and the molecular fluorescence lifetime of R6G is 3.7 ns, the total fluorescence duration to yield time-resolved images is estimated to be approximately 11 ns [34]. The R6G fluorescence from a cuvette is coupled into a single-mode fiber and a planoconvex lens (probe lens) is used to form an image of the fiber output near the trapping region. The particle shadows are imaged on an externally triggered CCD camera (Mightex) using a 10 \times long-working-distance infinity-corrected microscope objective and a conjugate $f = 200$ mm infinity-corrected tube lens. Laser light at 532 nm and 800 nm is blocked using a 550-nm long-pass filter and a 750-nm short-pass filter, respectively. The nanosecond laser is externally triggered from the femtosecond laser output Pockel cell with an interpulse delay of 200 μ s.

Shadowgraph images of the filament shock wave are captured by mounting a machine vision lens (MVL50M23, Navitar) to the CCD, yielding a magnification of $M = 0.903$. The position of the probe lens is adjusted to illuminate a larger area to accommodate the larger field of view. Each image is presented as a 100-shot average and the images are postprocessed through background subtraction, normalization, and a Gaussian blur filter to help extract the edges of the shock wave.

B. Optical trapping

For trapping, a cw 532-nm laser (Cobolt Samba, Hübner Photonics) with a maximum power of 1 W is used. Particles are trapped in a custom three-dimensionally printed chamber with small openings to pass the filament through without clipping or damaging the chamber. Particles are inserted using a pipette, with new particles being inserted periodically throughout the measurements. The chamber is decontaminated in an ultrasonic cleaner when changing out particles. The particle position is monitored in real time using a demagnified CCD camera [not shown in Fig. 1(a)] and shadowgraph images.

Graphite particles (3–5 μ m) are photophoretically trapped using a vertical hollow beam formed with dual-axicon lenses, focused using an aspheric lens with a numerical aperture (NA) of 0.66 as shown in Fig. 1(b). The aspheric lens is mounted on a vertical translation stage such that the height of the particles can be adjusted. Photophoretic trapping using a dual-axicon hollow beam has a tendency to trap multiple particles along the walls of the beam profile, in which case the most stable particle is isolated by slowly reducing the beam power [35].

Silica particles (2–6 μ m) are trapped using a confocal trapping configuration shown in Fig. 1(c), where a Gaussian beam is focused upward using a planoconvex lens with a NA of 0.51 that is refocused downward using a concave spherical mirror ($f = 10$ mm). By refocusing the beam downward, the upward radiation pressure is counteracted to yield a dominant gradient force that stabilizes particles near the confocal region. The height of the confocal-trapping region is adjusted by jointly moving both the lens and mirror. However, the particle position is not manipulated once it has been trapped, as slight movements easily destabilize the particle, and thus particles cannot be precisely positioned.

III. RESULTS AND DISCUSSION

A. Graphite displacement

Graphite particles displaced by the filament are shown in Fig. 2, where displacement is measured 200 μ s after the passage of the filament. Graphite particles are trapped using the hollow-beam configuration depicted in Fig. 1(b), and the position is manipulated with a vertical micrometer stage relative to the beam path of the filament. Starting from the most intense region of the filament core, the particles are positioned above and away from the filament at 100- μ m increments until the particles are no longer expelled from the trap at 500 μ m. The depth of field is approximately 3.6 μ m and thus many of the particles appear out of focus after they are displaced by the filament.

Particles trapped near the region of the filament core (0–100 μ m) in Figs. 2(a) and 2(b) are removed from the field of view (626×501 μ m) without traces of fragments. Similar observations are reported for water droplets, where

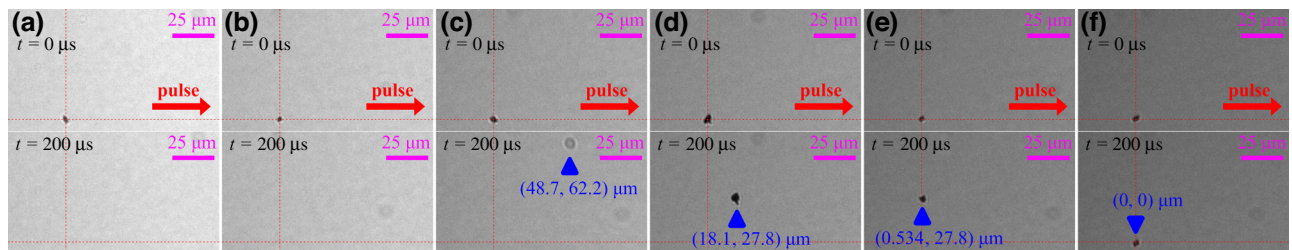


FIG. 2. Graphite particles displaced 200 μ s after interacting with a passing filament, placed (a) 0 μ m, (b) 100 μ m, (c) 200 μ m, (d) 300 μ m, (e) 400 μ m, and (f) 500 μ m away from the filament core.

droplets placed 100 μm from the filament are completely removed from displacement images through optical shattering and vaporization [28]. The intensity of the femtosecond pulse is the highest within the intensity-clamped filament core and thus particles located within this region, as in Fig. 2(a), are susceptible to morphological changes through laser ablation or damage. For graphite, damage to surface morphology can occur at laser energy fluences as low as $100 \text{ mJ}/\text{cm}^2$ using femtosecond pulses, with several studies reporting mass removal through the ejection of nanoclusters induced by strong laser-induced vibrations in the lattice structure [36–38]. At higher energy fluences exceeding $1 \text{ J}/\text{cm}^2$, mass removal through ablation can occur and can result in particle dissociation [36].

In order to compare the laser energy fluence of the filament to the damage and ablation threshold of graphite, a burn paper is used in the trapping region to measure the dimensions of the filament core and the surrounding energy reservoir, as shown in Fig. 3(a). The diameter of the filament core and that of the energy reservoir are measured to be $120 \mu\text{m}$ and $640 \mu\text{m}$, respectively. It is noted that the full width at half maximum (FWHM) diameter of the filament core would be lower than the measured diameter apparent on the burn paper. For the purpose of discussion, $120 \mu\text{m}$ will be assumed for the filament core diameter, as a conservative estimate for the laser energy fluence. The 1-m external focusing lens used in this experiment contributes to the beam convergence and results in a clamped intensity of $1.4 \times 10^{14} \text{ W}/\text{cm}^2$, such that the average energy fluence of the filament core is approximately $9.5 \text{ J}/\text{cm}^2$ for a Gaussian beam [39]. This far exceeds the ablation threshold of graphite and thus particles in the core are expected to dissociate through direct laser exposure and result in significant displacement through mass ejection of fragments. Under similar filament-energy-fluence conditions, emissions from the C_2 Swan system and CN violet system have been observed from ablating solid graphite samples as a result of vapor-phase mixing of C_2 with atmospheric species, supporting the view that graphite particles in the filament core can experience mass removal through ablation [40].

Particles residing between 200 and 300 μm away from the filament core, as in Figs. 2(c) and 2(d), are firmly in the region of the energy reservoir and experience both axial displacement along the beam path and transverse displacement away from the filament. The axial displacement is caused by interactions at the particle surface exposed to the light of the reservoir, such that particles located outside the radius of the energy reservoir ($320 \mu\text{m}$) do not experience any axial displacement, as in the cases of Figs. 2(e) and 2(f). Given the energy fluence and the dimensions of the filament core, approximately 50% of the pulse energy (1.8 mJ) constitutes the energy reservoir, neglecting significant losses from air ionization. For an energy-reservoir diameter of $640 \mu\text{m}$ with an inner hole

representative of the filament core, the average energy fluence is approximately $0.84 \text{ J}/\text{cm}^2$ and the energy fluence is expected to decrease closer to the outer boundaries of the energy reservoir [41,42]. As such, particles closer to the filament core experience a higher energy fluence and are displaced further along the beam path. To demonstrate, three different graphite particles are placed 200, 300, and 400 μm from the filament core (a total of nine particles), and the ratio between the axial and transverse displacement is measured in Fig. 3(b). Axial displacement through laser-induced forces predominates closer to the filament core due to the higher energy fluences. Conversely, particles outside of the boundaries of the energy reservoir experience negligible axial displacement, such that only transverse shock-wave-induced forces remain to displace the particles away from the filament.

The force induced by radiation pressure is expected to be a dominant contributor to the axial displacement of particles. Approximating the graphite particles as a completely absorptive and spherical body, the radiation pressure is

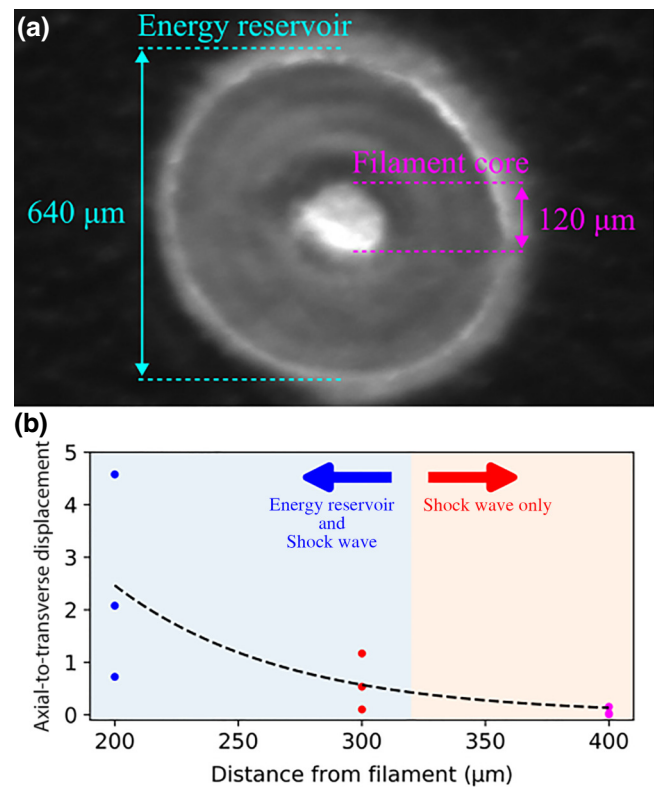


FIG. 3. (a) The transverse profile of the filament core and energy reservoir measured using a burn paper. (b) The axial-to-transverse displacement ratio measured for three different graphite particles trapped 200, 300, and 400 μm away from the filament core. Particles beyond the boundaries of the energy reservoir ($>320 \mu\text{m}$) only experience transverse displacement from the shock wave, resulting in a displacement ratio close to zero. An exponential function is fitted to guide the eye.

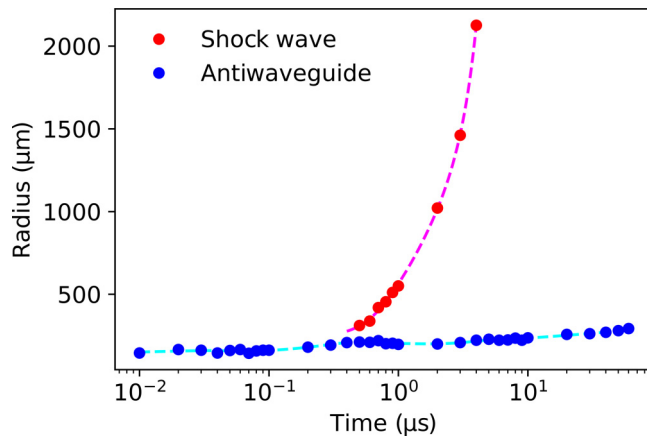


FIG. 4. The evolution of the filament shock wave and the antiwaveguide thermal channel captured using time-resolved shadowgraph images. Spline models are fitted to each trend to guide the eye [47].

$F_{rp} = IA_p/c$, where I is the irradiance of the light source, A_p is the cross-section area of the particle, and c is the speed of light. Based on the shadowgraph images, most of the trapped graphite particles have diameters ranging from 3 to 5 μm , resulting in a radiation pressure force ranging from 2.8 to 7.8 mN, given the average fluence of the energy reservoir. The force from radiation pressure calculated here is 1×10^6 times stronger than the reported transverse force induced by the shock wave for 4.82- μm silica placed 1 mm away from the filament, measured to be on the order of several nanonewtons [32]. For further comparison, the optical trapping laser with a NA of 0.66 at maximum power imparts a radiation pressure force of only 0.32 μN , which is sufficient to result in visible acceleration of particles during the trapping procedure.

The shock wave expands far beyond the boundaries of the energy reservoir, expanding to a radius of >1 mm within 2 μs , as shown in Fig. 4. As such, particles located more than 320 μm away from the filament will only experience a transverse shock-wave-induced force, as in the case of Fig. 2(e). The three particles measured at 400 μm in Fig. 2(e) are displaced by 24–35 μm by the shock wave alone. Relative to the dimensions of the filament core (120 μm), the measured displacement of particles by the shock wave indicates that filaments are capable of clearing air channels devoid of atmospheric debris to improve transmission of subsequent femtosecond pulses or secondary light sources. However, the shadowgraph images also reveal a persisting thermal antiwaveguide, which—to the detriment of transmitting light through the cleared air channel—will refract light outward without the use of structured waveguides [29,43–46].

The images in Figs. 2(c) and 2(d) and the particle images used in Fig. 3(b) do not show any indication of fragmentation in the particle morphology. It is possible that

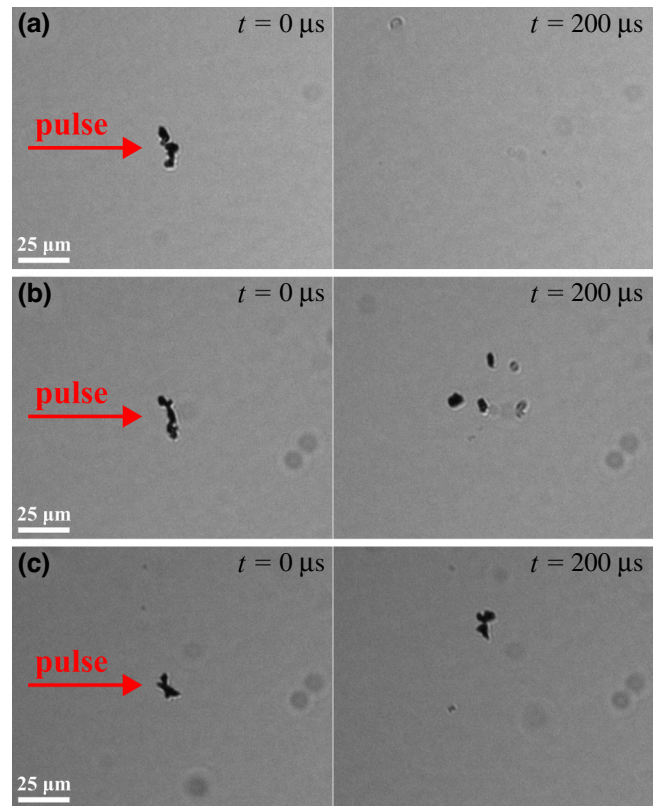


FIG. 5. Graphite deagglomeration imaged 200 μs after interacting with a passing filament for particles positioned (a) 200 μm and (b) 300 μm from the filament core. At (c) 400 μm , the agglomerate is outside the boundaries of the energy reservoir and only experiences transverse displacement from the shock wave.

nanoclusters are ejected from the irradiated surface but are simply unresolved or out of focus, given that the energy fluence of the energy reservoir exceeds the damage threshold for graphite that is reported to result in mass ejecta in solid samples [36–38]. However, the filament is found to be capable of breaking apart larger particle agglomerates, as shown in Figs. 5(a) and 5(b). The individual fragments ejected from the agglomerates are displaced further from their original positions the closer they are to the filament core, indicating that deagglomeration is driven mainly by direct exposure to laser light. This is further supported by the axial-to-transverse displacement ratios in Fig. 3(b), where a ratio larger than 1 indicates that radiation pressure (axial displacement) imparts more energy to the particles than the shock wave (transverse displacement). Agglomerates outside of the energy reservoir, as in the case of Fig. 5(c), are transversely displaced by the shock wave alone, similar to the single particles in Fig. 2(e), but remain largely intact. Both acceleration from radiation pressure and acceleration from shock-wave pressure are inversely proportional to the diameter of the particle and thus deagglomeration is expected to improve the particle displacement induced by subsequent pulses.

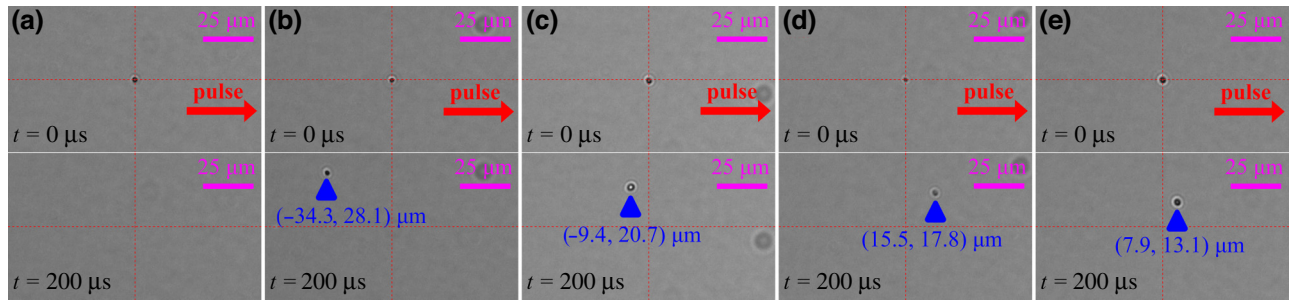


FIG. 6. Silica particles displaced 200 μs after interacting with a passing filament. The initial distance to the filament core is measured to be (a) 64 μm , (b) 72 μm , (c) 140 μm , (d) 205 μm , and (e) 306 μm .

B. Silica displacement

Silica microspheres (2–6 μm) are trapped using the confocal-trapping configuration shown in Fig. 1(c) with a Gaussian beam. The position of the particle is no longer manipulated but, instead, particles are trapped near the filament core and the relative distance to the filament is measured. The densities of silica and graphite are 2.65 g/cm^3 and 2.26 g/cm^3 , respectively. Given the similar particle-size distributions, the mass of each individual particle is comparable. Characteristic displacement behaviors for silica are selected and presented in Fig. 6.

Similar to graphite, the silica particles experience outward transverse displacement from interacting with the shock wave. The silica particle 64 μm away from the filament core in Fig. 6(a) is removed from the field of view much like the graphite in Figs. 2(a) and 2(b), possibly as a result of ablation. The ablation and damage thresholds of silica are higher than those of graphite, at 3.5 J/cm^2 and 2.5 J/cm^2 , respectively [48]. Nonetheless, the average fluence of the filament core (9.5 mJ/cm^2) is still higher than the ablation threshold of silica and thus particle dissociation is expected to occur.

Particles located 72–140 μm from the filament core are axially displaced backward, as shown in Figs. 6(b) and 6(c). This behavior is similar to optical shattering observed for water droplets caused by cavitation and ejection of mass from the rear surface of the droplet, resulting in backward axial displacement [28]. Both silica and water are mostly transparent to 800-nm laser light, such that it is feasible that a similar optical shattering phenomenon can occur; however, a higher energy fluence is required to shatter silica, as mass ejection cannot occur by disrupting surface tension and would instead require morphological damage to occur close to the rear surface of the particle. The average fluence of the energy reservoir (0.84 mJ/cm^2) is lower than the damage threshold of silica (2.5 mJ/cm^2) and thus the irradiated front surface of the particle is expected to remain intact. Light irradiating the front surface of the silica particle is expected to internally focus, increasing the energy fluence as the light propagates through the particle toward the rear surface.

To estimate the fluence at the rear surface, silica microspheres are modeled using ray-transfer matrices for a thick lens with a radius of curvature equivalent to the particle radius with incident parallel rays. Assuming a constant transmission of 90%, the energy fluence at the rear surface is greater by a factor of 6.26 compared to the front irradiated surface, such that the energy-reservoir fluence of 0.84 mJ/cm^2 incident at the front surface will be focused and increased to 5.3 mJ/cm^2 . The fluence at the rear surface is higher than both the damage and ablation thresholds of silica, supporting the view that silica particles can eject mass localized near the rear surface to undergo optical shattering and propel the particle backward.

Particles that are not optically shattering are axially displaced along the direction of the beam path, as shown in Figs. 6(d) and 6(e). Without mass being ejected at the rear surface, backward displacement cannot occur, leaving only the forward momentum imparted from scattered light. The silica particles in Figs. 6(d) and 6(e) are not displaced as far as the graphite particles in Figs. 2(c) and 2(d) at similar distances from the filament core, indicating that radiation pressure is lower for silica and other transparent particles. The reflected light at the particle surface results in radiation pressure that is twice as strong compared to absorbed light. Assuming a negligible contribution from absorption and 10% reflectivity, the radiation-pressure force experienced by silica particles is approximately a factor of 5 lower than for graphite particles of equivalent size. Thus, particles that are transparent to the laser light and that remain intact after exposure are expected to experience limited axial displacement compared to absorptive particles.

IV. CONCLUSIONS

Using time-resolved shadowgraph images of displaced optically trapped particles, laser filaments are demonstrated to be capable of clearing solid atmospheric debris consisting of micrometer-sized particles. Particles are displaced in both axial and transverse directions from laser-induced forces and the shock-wave-induced force, respectively. The shock wave rapidly propagates beyond

the boundaries of the energy reservoir and is capable of displacing particles by more than 10 μm , suggesting that the filament can clear a channel larger than the diameter of the energy reservoir (640 μm) to improve transmission of subsequent pulses or secondary light sources. Axial displacement along the axis of the beam path is driven by interaction of particles with the high-intensity region of the filament core or the low-intensity region of the energy reservoir from direct laser exposure. As a result, the optical properties of the particle will heavily influence clearing mechanisms induced by laser interactions, which is demonstrated using graphite and silica particles to represent absorptive and transparent atmospheric debris. Absorptive particles will experience localized energy deposition at the irradiated surface to propel the particles along the beam path through mass ejection and radiation pressure. Furthermore, it is shown that the energy fluence of the energy reservoir is sufficiently high to break apart graphite-particle agglomerates. Given that the acceleration from the shock wave and the radiation pressure are inversely proportional to the particle size, deagglomeration is expected to improve debris clearing by reducing the particle-size distribution for subsequent pulses. Transparent particles can internally focus light to expel mass from the rear surface of the particle through ablation or mechanical damage, propelling the particle backward against the beam path through optical shattering. Optical shattering is observed to occur only for particles close to the filament core, where the energy fluence is expected to be higher than the ablation or damage threshold of the particle after internal focusing. Silica particles further away from the filament core ($>200 \mu\text{m}$) are propelled forward along the beam path like graphite, indicating that the particle is largely unaffected by optical shattering, leaving only the forward momentum imparted from scattered light. Given that the shock wave directly pushes particles away from the filament, the implication with regard to atmospheric particle clearing is intuitive. Over several shots, transmission is expected to improve as long as the period of the pulse train is shorter than the recovery time of the aerosol. However, the consequence of axially displacing particles along the beam path through radiation pressure and optical shattering largely remains unknown for both droplets and solid particles. Given that the axial forces are increased at higher energy fluences, the particle concentrations are expected to be reduced closer to the filament core, as they are axially displaced to lower-fluence regions; however, accurately determining particle transport over several shots would require complete knowledge of the energy distribution along the length of the filament. Furthermore, while two extreme cases are presented by investigating the axial displacement between graphite and silica, realistically most atmospheric particles are semitransparent or semiabsorptive and would require further study

to characterize their displacement mechanisms in a laser filament.

ACKNOWLEDGMENTS

This work is the result of research funded partially by the U.S. Department of Defense Science, Mathematics, and Research for Transformation (SMART) Scholarship-for-Service Program; U.S. Department of Energy (DOE) National Nuclear Security Administration Consortium for Nuclear Forensics Award No. DE-NA0004142; and Defense Threat Reduction Agency Award No. HDTRA1-20-2-0002. The content of the information does not necessarily reflect the position or the policy of the federal government, and no official endorsement should be inferred.

-
- [1] W. Liu and S. L. Chin, Direct measurement of the critical power of femtosecond Ti:sapphire laser pulse in air, *Opt. Express* **13**, 5750 (2005).
 - [2] A. Becker, N. Aközbeç, K. Vijayalakshmi, E. Oral, C. Bowden, and S. Chin, Intensity clamping and re-focusing of intense femtosecond laser pulses in nitrogen molecular gas, *Appl. Phys. B* **73**, 287 (2001).
 - [3] H. Xu, A. Azarm, J. Bernhardt, Y. Kamali, and S. Chin, The mechanism of nitrogen fluorescence inside a femtosecond laser filament in air, *Chem. Phys.* **360**, 171 (2009).
 - [4] M. Mlejnek, E. Wright, and J. Moloney, Dynamic spatial replenishment of femtosecond pulses propagating in air, *Opt. Lett.* **23**, 382 (1998).
 - [5] Z. Hao, J. Zhang, X. Lu, T. Xi, Z. Zhang, and Z. Wang, Energy interchange between large-scale free propagating filaments and its background reservoir, *J. Opt. Soc. Am. B* **26**, 499 (2009).
 - [6] T. Fujii, N. Goto, M. Miki, T. Nayuki, and K. Nemoto, Lidar measurement of constituents of microparticles in air by laser-induced breakdown spectroscopy using femtosecond terawatt laser pulses, *Opt. Lett.* **31**, 3456 (2006).
 - [7] J.-F. Daigle, P. Mathieu, G. Roy, J.-R. Simard, and S. Chin, Multi-constituents detection in contaminated aerosol clouds using remote-filament-induced breakdown spectroscopy, *Opt. Commun.* **278**, 147 (2007).
 - [8] Z. Zhang, N. Zhang, Y. Wang, B. Xie, Y. Xiang, J. Guo, B. Shang, L. Guo, X. Zhao, M. Xie, L. Lin, and W. Liu, Detection of $1.4 \mu\text{g}/\text{m}^3 \text{Na}^+$ in aerosol at a 30 m distance using 1 kHz femtosecond laser filamentation in air, *Opt. Express* **31**, 6464 (2023).
 - [9] K. S. Latty, M. Burger, J. Borrero, I. Jovanovic, and K. C. Hartig, Emission characteristics of bulk aerosols excited by externally focused femtosecond filaments, *Opt. Express* **31**, 24652 (2023).
 - [10] J. Kasparian, M. Rodriguez, G. Méjean, J. Yu, E. Salmon, H. Wille, R. Bourayou, S. Frey, Y.-B. André, A. Mysyrowicz, R. Sauerbrey, J.-P. Wolf, and L. Wöste, White-light filaments for atmospheric analysis, *Science* **301**, 61 (2003).
 - [11] G. Mejean, J. Kasparian, J. Yu, S. Frey, E. Salmon, and J.-P. Wolf, Remote detection and identification of biological

- aerosols using a femtosecond terawatt lidar system, *Appl. Phys. B: Lasers Opt.* **78**, 535 (2004).
- [12] H. L. Xu and S. L. Chin, Femtosecond laser filamentation for atmospheric sensing, *Sensors* **11**, 32 (2010).
- [13] O. A. Bukin, M. Y. Babii, S. S. Golik, A. A. Il'in, A. M. Kabanov, A. V. Kolesnikov, Y. N. Kulchin, V. V. Lisitsa, G. G. Matvienko, V. K. Oshlakov, and K. A. Shmirko, Lidar sensing of the atmosphere with gigawatt laser pulses of femtosecond duration, *Quantum Elec.* **44**, 563 (2014).
- [14] F. Courvoisier, V. Boutou, J. Kasparian, E. Salmon, G. Méjean, J. Yu, and J.-P. Wolf, Ultraintense light filaments transmitted through clouds, *Appl. Phys. Lett.* **83**, 213 (2003).
- [15] M. Kolesik and J. V. Moloney, Self-healing femtosecond light filaments, *Opt. Lett.* **29**, 590 (2004).
- [16] A. Dubietis, E. Kučinskas, G. Tamošauskas, E. Gaižauskas, M. A. Porras, and P. Di Trapani, Self-reconstruction of light filaments, *Opt. Lett.* **29**, 2893 (2004).
- [17] L. de la Cruz, E. Schubert, D. Mongin, S. Klingebiel, M. Schultze, T. Metzger, K. Michel, J. Kasparian, and J.-P. Wolf, High repetition rate ultrashort laser cuts a path through fog, *Appl. Phys. Lett.* **109**, 251105 (2016).
- [18] G. Schimmel, T. Produit, D. Mongin, J. Kasparian, and J.-P. Wolf, Free space laser telecommunication through fog, *Optica* **5**, 1338 (2018).
- [19] A. Higginson, Y. Wang, H. Chi, A. Goffin, I. Larkin, H. M. Milchberg, and J. J. Rocca, Wake dynamics of air filaments generated by high-energy picosecond laser pulses at 1 kHz repetition rate, *Opt. Lett.* **46**, 5449 (2021).
- [20] A. D. Koulouklidis, C. Lanara, C. Daskalaki, V. Y. Fedorov, and S. Tzortzakis, Impact of gas dynamics on laser filamentation THz sources at high repetition rates, *Opt. Lett.* **45**, 6835 (2020).
- [21] M. C. Schroeder, I. Larkin, T. Produit, E. W. Rosenthal, H. Milchberg, and J.-P. Wolf, Molecular quantum wakes for clearing fog, *Opt. Express* **28**, 11463 (2020).
- [22] S. Zahedpour, J. Wahlstrand, and H. Milchberg, Quantum control of molecular gas hydrodynamics, *Phys. Rev. Lett.* **112**, 143601 (2014).
- [23] W.-F. Hsieh, J.-B. Zheng, C. F. Wood, B. T. Chu, and R. K. Chang, Propagation velocity of laser-induced plasma inside and outside a transparent droplet, *Opt. Lett.* **12**, 576 (1987).
- [24] J. C. Carls and J. R. Brock, Propagation of laser breakdown and detonation waves in transparent droplets, *Opt. Lett.* **13**, 273 (1988).
- [25] J.-b. Zheng, W.-F. Hsieh, S.-c. Chen, and R. K. Chang, Temporally and spatially resolved spectroscopy of laser-induced plasma from a droplet, *Opt. Lett.* **13**, 559 (1988).
- [26] A. Lindinger, J. Hagen, L. D. Socaciu, T. M. Bernhardt, L. Wöste, D. Duft, and T. Leisner, Time-resolved explosion dynamics of H₂O droplets induced by femtosecond laser pulses, *Appl. Opt.* **43**, 5263 (2004).
- [27] C. Jeon, D. Harper, K. Lim, M. Durand, M. Chini, M. Baudelet, and M. Richardson, Interaction of a single laser filament with a single water droplet, *J. Opt.* **17**, 055502 (2015).
- [28] A. Goffin, J. Griff-McMahon, I. Larkin, and H. Milchberg, Atmospheric aerosol clearing by femtosecond filaments, *Phys. Rev. Appl.* **18**, 014017 (2022).
- [29] N. Jhajji, E. Rosenthal, R. Birnbaum, J. Wahlstrand, and H. Milchberg, Demonstration of long-lived high-power optical waveguides in air, *Phys. Rev. X* **4**, 011027 (2014).
- [30] O. Lahav, L. Levi, I. Orr, R. A. Nemirovsky, J. Nemirovsky, I. Kaminer, M. Segev, and O. Cohen, Long-lived waveguides and sound-wave generation by laser filamentation, *Phys. Rev. A* **90**, 021801 (2014).
- [31] G. Point, E. Thouin, A. Mysyrowicz, and A. Houard, Energy deposition from focused terawatt laser pulses in air undergoing multifilamentation, *Opt. Express* **24**, 6271 (2016).
- [32] M. C. Schroeder, U. Andral, and J.-P. Wolf, Optomechanical expulsion of individual micro-particles by laser-induced shockwave in air, *AIP Adv.* **12**, 095119 (2022).
- [33] S. L. Chin, A. Brodeur, S. Petit, O. G. Kosareva, and V. P. Kandidov, Filament and supercontinuum generation during the propagation of powerful ultrashort laser pulses in optical media (white light laser), *J. Nonlinear Opt. Phys. Mater.* **08**, 121 (1999).
- [34] K. A. Selanger, J. Falnes, and T. Sikkeland, Fluorescence lifetime studies of Rhodamine 6G in methanol, *J. Phys. Chem.* **81**, 1960 (1977).
- [35] T. Liu, X. Cheng, Q. Zhang, T. Zhang, and J. Bai, Improvement of the reproducibility in LIBS single levitated aerosol particle analysis based on particle size-selectivity of photophoretic optical trap, *Talanta* **268**, 125326 (2024).
- [36] S. Amoroso, G. Ausanio, M. Vitiello, and X. Wang, Infrared femtosecond laser ablation of graphite in high vacuum probed by optical emission spectroscopy, *Appl. Phys. A* **81**, 981 (2005).
- [37] M. Lenner, A. Kaplan, C. Huchon, and R. E. Palmer, Ultrafast laser ablation of graphite, *Phys. Rev. B* **79**, 184105 (2009).
- [38] A. A. Ionin, S. I. Kudryashov, S. V. Makarov, N. N. Mel'nik, P. N. Saltuganov, L. V. Seleznev, and D. V. Sinit'syn, Ultrafast femtosecond laser ablation of graphite, *Laser Phys. Lett.* **12**, 075301 (2015).
- [39] S. I. Mityukovskiy, Y. Liu, A. Houard, and A. Mysyrowicz, Re-evaluation of the peak intensity inside a femtosecond laser filament in air, *J. Phys. B: At., Mol. Opt. Phys.* **48**, 094003 (2015).
- [40] E. J. Judge, G. Heck, E. B. Cerkez, and R. J. Levis, Discrimination of composite graphite samples using remote filament-induced breakdown spectroscopy, *Anal. Chem.* **81**, 2658 (2009).
- [41] A. Couairon and L. Bergé, Light filaments in air for ultraviolet and infrared wavelengths, *Phys. Rev. Lett.* **88**, 135003 (2002).
- [42] X.-L. Liu, W. Cheng, M. Petrarca, and P. Polynkin, Measurements of fluence profiles in femtosecond laser filaments in air, *Opt. Lett.* **41**, 4751 (2016).
- [43] M. Alshershby, Z. Hao, A. Camino, and J. Lin, Modeling a femtosecond filament array waveguide for guiding pulsed infrared laser radiation, *Opt. Commun.* **296**, 87 (2013).

- [44] M. Châteauneuf, S. Payeur, J. Dubois, and J.-C. Kieffer, Microwave guiding in air by a cylindrical filament array waveguide, *Appl. Phys. Lett.* **92**, 091104 (2008).
- [45] P. J. Skrodzki, M. Burger, L. A. Finney, R. Nawara, J. Nees, and I. Jovanovic, Millisecond-long suppression of spectroscopic optical signals using laser filamentation, *Opt. Lett.* **46**, 3777 (2021).
- [46] S. B. Ali Reza, M. Burger, P. Bassène, T. Nutting, I. Jovanovic, and M. N’Gom, Generation of multiple obstruction-free channels for free space optical communication, *Opt. Express* **31**, 3168 (2023).
- [47] See the Supplemental Material at <http://link.aps.org/supplemental/10.1103/PhysRevApplied.22.014075> for the images used to capture the evolution of the filament shock wave and thermal antiwaveguide channel. Each frame of the filament evolution is averaged over 100 shots and background subtracted for better clarity prior to edge extraction.
- [48] B. Chimier, O. Utéza, N. Sanner, M. Sentis, T. Itina, P. Lassonde, F. Légaré, F. Vidal, and J. C. Kieffer, Damage and ablation thresholds of fused-silica in femtosecond regime, *Phys. Rev. B* **84**, 094104 (2011).